Nano Today 28 (2019) 100768

Contents lists available at ScienceDirect

Nano Today

journal homepage: www.elsevier.com/locate/nanotoday

Review

Facet-dependent and interfacial plane-related photocatalytic behaviors of semiconductor nanocrystals and heterostructures

Michael H. Huang*, Mahesh Madasu

Department of Chemistry and Frontier Research Center on Fundamental and Applied Sciences of Matters, National Tsing Hua University, Hsinchu 30013, Taiwan

ARTICLE INFO

Article history:
Received 1 April 2019
Received in revised form 31 July 2019
Accepted 13 August 2019
Available online 23 August 2019

Keywords:
Facet-dependent properties
Heterojunctions
Interfacial charge transfer
Nanocrystals
Photocatalytic activity
Semiconductors

ABSTRACT

Recent studies on polyhedral semiconductor nanocrystals and semiconductor wafers have revealed that their electronic and photocatalytic properties are highly facet-dependent. For example, Cu_2O rhombic dodecahedra are highly photocatalytically active, but cubes are inactive. Through density functional theory (DFT) calculations, these observations can be understood because different crystal surface planes display variable band structures, giving rise to tunable degrees of valence and conduction band bending and difficulty to charge carrier migration across these surfaces. In the case of Cu_2O cubes, the observed photocatalytic inactivity results from a large barrier height at the {100} face, preventing charge carriers from moving past this crystal surface. Remarkably, growing another semiconductor such as ZnO, CdS, ZnS, or Ag_3PO_4 nanostructures on Cu_2O cubes, octahedra, and rhombic dodecahedra often lead to varying degrees of photocatalytic activity suppression, rather than the expected enhancement. These studies have suggested that the specific contacting lattice planes at the heterojunction can significantly affect charge carrier transport across the interface through a large degree of interfacial band bending, meaning the outcome of photocatalytic activity is highly interfacial plane-related. Such insights are quite important, and imply that solar cells and heterostructured photocatalyst designs need to pay attention to such effects to effectively improve their performance. This Review largely uses examples from our work to illustrate recent advances in the understanding of facet-dependent electronic and photocatalytic properties of semiconductor materials.

Contents

Introduction

The formation of semiconductor nanocrystals with well-defined shapes including TiO_2, Cu_2O, Ag_2O, PbS, Ag_3PO_4, and $SrTiO_3$ has enabled the examinations of their electrical conductivity and photocatalytic properties toward dye degradation, water splitting, and CO_2 reduction reactions with respect to the exposed crystal faces [1–8]. Very large differences in surface-related electrical conductivity and photocatalytic activity behaviors have been recorded, showing this is truly an interesting and important research topic to pursue for better understanding of semiconductor materi-

* Corresponding author.
E-mail address: hyhuang@mx.nthu.edu.tw (M.H. Huang).

https://doi.org/10.1016/j.nantod.2019.100768
1748-0132/

als and their applications. Cu_2O crystals also appear to show facet-dependent electrochemical methanol oxidation properties [9]. Moreover, facet-dependent organic coupling reactions such as click and alkyne hydroboration reactions using polyhedral Cu_2O catalysts have been explored, revealing rhombic dodecahedra as generally a superior catalyst [10–12]. Metal oxides such as CeO_2 and Co_3O_4 with shape control have also been widely studied for CO oxidation [13]. Light-induced surface hydrophilicity has also been examined for different faces of ZnO and TiO_2 crystals [14,15]. In contrast to the facet-dependent organocatalytic properties of these semiconductor nanocrystals, which consider mainly interactions between molecules and various crystal surfaces, facet-dependent electrical and photocatalytic behaviors of semiconductors are related to the presence of an ultrathin surface layer of finite thickness with dissimilar band structures for different surface planes, and involve charge carriers moving into and out of a crystal through its surfaces [16–21]. Thus, surface atomic arrangement is not useful for predicting electrical and photocatalytic behaviors. If surface plane-dependent band bending is a general property of semiconductors, it is then possible that each component of a semiconductor heterojunction can has its own interfacial band bending. This means that the outcome of photocatalytic activity in semiconductor heterostructures is not always predictable as generally believed by researchers on the basis of band alignment analysis, and suppression should be observable in some unfavorable contacting plane combinations. This appears to be true, but this fact is rarely reported. Broadly speaking, solar cells often contain many semiconductor heterojunctions, so interfacial planes to charge transport should be more widely studied as an effective approach to efficiency enhancement [22–24]. And GaN/InGaN LEDs (light-emitting diodes) should result from facet-dependent efficient charge migration across multiple semiconductor interfaces to produce bright blue light, even though we generally do not think of its success this way [25,26]. In this sense, we already benefit from the power of semiconductor facet effects. This Review begins with electrical conductivity measurements of various semiconductor materials to show that electronic properties of semiconductors are generally facet-dependent. Such behaviors can be understood recognizing their surface band structures are tunable with respect to the exposed crystal faces. Similarly, the surface band structure-induced variable degrees of band bending lead to the observation of strongly facet-dependent photocatalytic activities. Here Cu_2O and Ag_2O are excellent examples to illustrate how band structure differences are quite useful to explain their opposite trends in facet-dependent photocatalytic activity. Finally, photocatalytic activity enhancement and suppression of several Cu_2O-based semiconductor heterostructures with plane-specific interfaces is discussed. Recognizing photocatalytic deactivation of semiconductor heterojunctions with perceived favorable band alignment, instead of expected enhancement, can still happen is important to our better understanding of semiconductors. We can also view this as presenting opportunities to fabricate novel semiconductor structures with useful properties.

Facet-dependent electrical conductivity properties of semiconductor nanocrystals and wafers

Back in 2011, electrical conductivity measurements on a single {100}-bound Cu_2O cube and {111}-bound octahedron were reported by contacting a particle with tungsten probes connected to a nanomanipulator [27]. Very large conductivity differences between these two faces of Cu_2O have been recorded. With the availability of Cu_2O rhombic dodecahedra exposing only the {110} faces, the three particle shapes were measured again [16]. Fig. 1a gives the collected *I-V* curves, showing a Cu_2O octahedron is highly conductive, while a cube is moderately conductive, and a rhombic dodecahedron is non-conductive. Thus, a Cu_2O crystal can behave like a metal, a semiconductor, and an insulator. When tungsten probes were brought to contact two different facets of a Cu_2O particle such as a cuboctahedron, asymmetric *I-V* curves were obtained, suggesting a single particle can act as a *p–n* junction for current rectification. Because this is mainly a surface effect, a modified band diagram was drawn to show tunable degrees of band bending for various crystal faces (Fig. 1b). Cu_2O is a *p*-type semiconductor, so holes are considered as the charge carriers. The non-conductive {110} face has the largest band bending to represent its biggest barrier to charge transport across this face when contacted with W, while the {111} face should have the least degree of band bending to facilitate charge migration. Use of ultraviolet photoelectron spectroscopy for valence band position and UV–vis spectroscopy for conduction band position to construct band diagrams of the three Cu_2O crystal shapes has yielded similar band energies, explaining why conventional approach is unable to explain the measured large conductivity differences [28]. To substantiate the existence of this thin surface layer giving the observed electrical facet effects, DFT calculations on tunable number of Cu_2O lattice planes were performed. Fig. 1c provides the resultant electron density of states (DOS) plots for 3 layers of Cu_2O (111), (100), and (110) planes, showing no energy gap above the Fermi level at 0 eV for the (111) planes and a clear gap for the (110) planes. The (100) plane case is intermediate of the two cases. These DOS plots match well with experimental measurements. Next, the number of plane layers was varied to see at which point a gap is developed, and this represents the layer thickness responsible for the observed facet-dependent properties. The layer thickness is about 1 nm or less for different surfaces of Cu_2O [16]. Subsequently, electrical conductivity measurements on single TiO_2, PbS, Ag_2O, and Ag_3PO_4 crystals were conducted, showing they all possess facet-dependent electrical conductivity properties [4,5,17,18,29]. Fig. 1d offers the collected *I-V* curves for a single Ag_2O cube, octahedron, and rhombic dodecahedron. The conductivity trend is same as that of Cu_2O, but the {111} faces are not as conductive, and the least conductive {110} faces still show some conductivity. For PbS, the conductivity variation for different crystal faces are not as large as that seen in Ag_2O, so every material has its own conductivity characteristics.

In addition to nanoscale crystals, Si and Ge wafers also exhibit facet-dependent electronic properties. Using non-doped intrinsic {100} and {111} Si and Ge wafers, sharp cuts parallel and perpendicular to the flat edge of the wafers were made to expose {110} and {211} surfaces for complete electrical conductivity measurements [30,31]. In agreement with DFT calculations, Si and Ge {111} and {211} faces are much more conductive than {100} and {110} faces. When electrical contacts were made simultaneously on the {111} and {110} faces, asymmetric current-rectifying *I-V* responses were obtained (Fig. 1e). Further calculations revealed notable variations in the Si–Si (and Ge–Ge) bond length, bond geometry, and frontier orbital electron distribution within the thin surface layer of (111) and (211) planes from the semiconducting (100) and (110) plane cases, suggesting the origin of facet-dependent electrical behaviors is quantum mechanical in nature at the orbital level. These examples indicate that facet-dependent electronic properties of semiconductors are broadly observable from nanoscale particles to wafer-sized structures. Recently, it has been shown that when a voltage is applied to a p-type Cu_2O octahedron deposited on an n-type Si substrate through the use of an atomic force microscopy (AFM) probe, rectifying *I-V* curves were recorded [32,33]. Somewhat asymmetric *I-V* characteristic was also obtained when Cu_2O/TiO_2 heterojunctions were measured [34]. Hence, the contacting interfaces can be investigated for facet-dependent electronic responses, and this should expand our knowledge of semiconductor properties for potential applications.

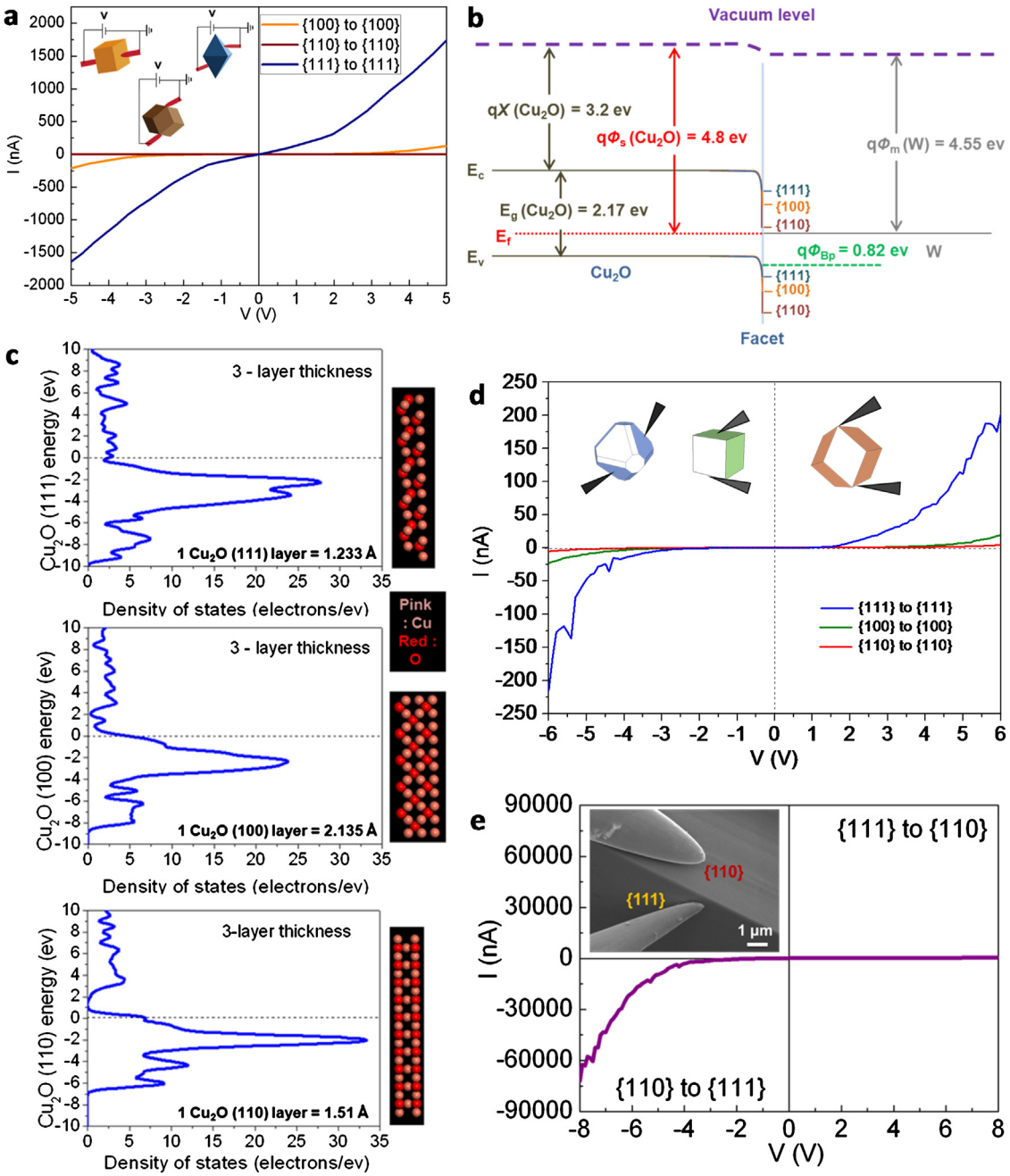

Fig. 1. (a) *I–V* curves for the {100}, {110}, and {111} faces of a single Cu_2O cube, rhombic dodecahedron, and octahedron. Electrical connections are also shown. (b) Adjusted band diagram of Cu_2O with consideration of relative band edge energies of different crystal faces. (c) DOS plots for the (111), (100), and (110) planes of Cu_2O consisting of three layers of these planes. (a–c) Printed with permission from Ref. [16] Copyright (2015) American Chemical Society. (d) *I-V* curves for the {111}, {100}, and {110} faces of Ag_2O crystals. Printed with permission from Ref. [17] Copyright (2017) Wiley-VCH. (e) SEM image showing tungsten probes contacting Si {111} and {110} faces and the recorded *I-V* curve. Printed with permission from Ref. [30] copyright (2017) Wiley-VCH.

Facet-dependent photocatalytic properties of Cu_2O, Ag_2O, and Ag_3PO_4 crystals

Although some oxide semiconductors including CeO_2 and α-Fe_2O_3 have been shown to display facet-dependent photocatalytic or photoelectrochemical behaviors [1,35–37], Cu_2O with a body-centered cubic crystal structure is likely the most widely studied material for facet effects to photocatalysis. This popularity results from the ability to synthesize Cu_2O nanocrystals with diverse shapes. It has been reported that Cu_2O rhombic dodecahedra are much more photocatalytically active than octahedra, while cubes are inactive [38–41]. However, Cu_2O cubes have also been shown to display some photocatalytic activity [27,42–44]. Possible reasons for this confusion include the formation of imperfect cubes, presence of some Cu_2O particles that are not exactly cubic, and surface oxidation to give CuO. Even deposition of Au particles on Cu_2O cubes without adding a reducing agent can inadvertently and unknowingly change the {100} faces of Cu_2O, making the cubes to appear photocatalytically active [41]. To confirm photocatalytic inactivity of Cu_2O cubes, Au nanoparticles were sparsely grown on Cu_2O cubes, octahedra, and rhombic dodecahedra by introducing ascorbic acid as a reducing agent to reduce $HAuCl_4$ to Au [45]. The idea was to enhance photocatalytic activity through Au decoration as a cocatalyst to facilitate photogenerated electron and hole sepa-

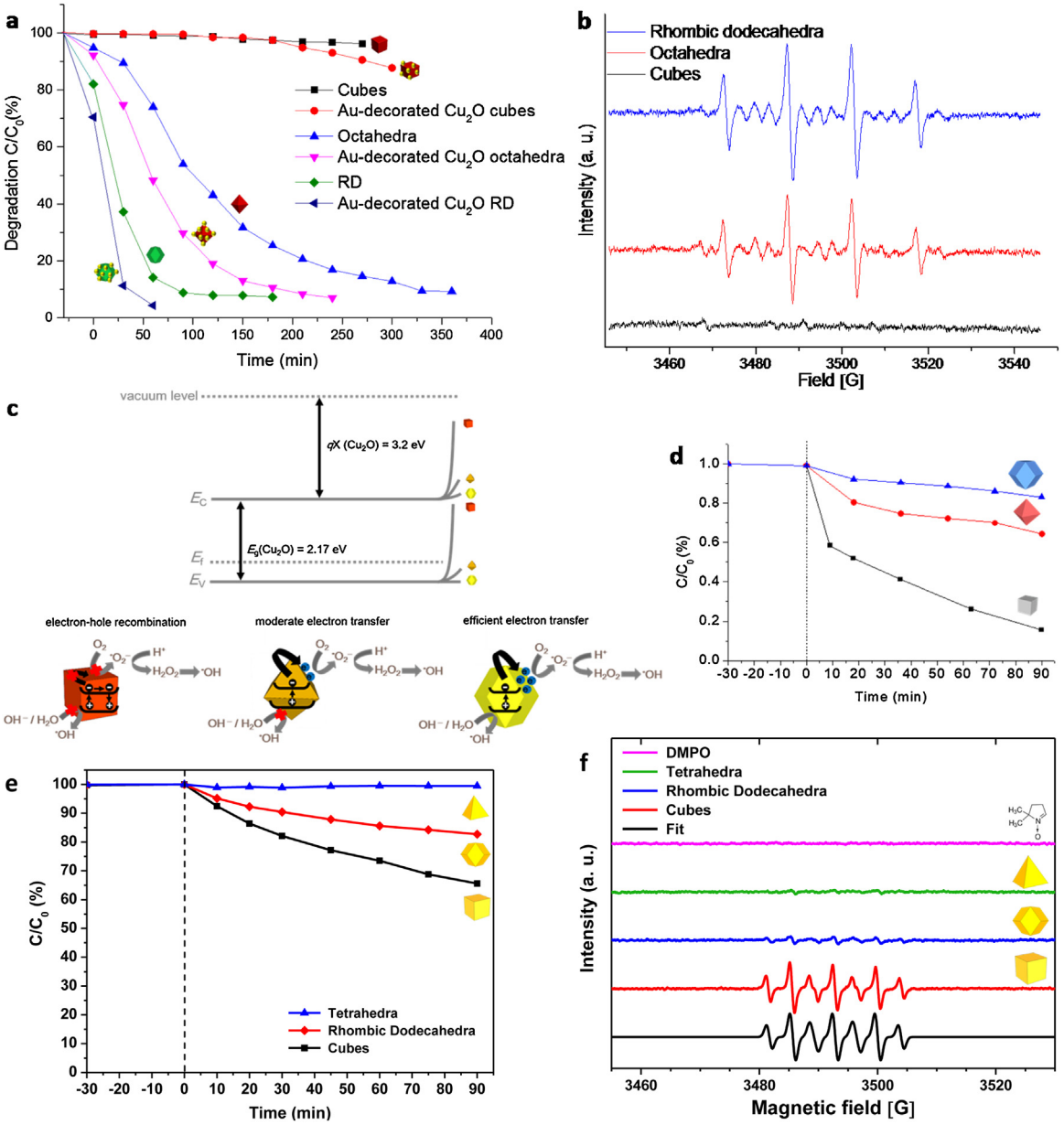

Fig. 2. (a) Photodegradation of methyl orange as a function of time for the various Cu_2O crystals and Au-decorated Cu_2O heterostructures. (b) EPR spectra of DMPO-OH present in photoirradiated Cu_2O cubes, octahedra, and rhombic dodecahedra. (a and b) Printed with permission from Ref. [45] copyright (2016) Wiley-VCH. (c) Band diagram of Cu_2O presenting different degrees of band bending for different crystal surfaces to account for their photocatalytic behaviors. The drawings show different photocatalytic responses for Cu_2O cubes, octahedra, and rhombic dodecahedra. Printed with permission from Ref. [28] copyright (2017) Royal Society of Chemistry. (d) MO photodegradation extent versus reaction time for Ag_2O cubes, octahedra, and rhombic dodecahedra. Printed with permission from Ref. [47] Copyright (2016) American Chemical Society. (e) Extents of methyl orange photodegradation as a function of reaction time using various Ag_3PO_4 crystals as the photocatalysts. (f) EPR spectra of DMPO-OH in the presence of photoirradiated Ag_3PO_4 crystals. Printed with permission from Ref. [29] Copyright (2017) American Chemical Society.

ration. As seen in Fig. 2a, Au-decorated Cu_2O octahedra and rhombic dodecahedra indeed improved their photocatalytic performance, but Au-decorated Cu_2O cubes remained inactive. The slight activity recorded after 3 h of photoirradiation was due to the formation of CuO as revealed by X-ray photoelectron spectroscopy (XPS) analysis. Interestingly, while Cu_2O octahedra can form edge depression and some rhombic dodecahedra can show surface deformation upon extended light illumination, their structural stability has greatly improved after Au nanoparticle deposition. This enhanced stability may be due to more effective removal of photogenerated holes to limit oxidation of Cu_2O crystals [45].

Using DMPO to capture hydroxyl ($^{\bullet}OH$) and superoxide ($^{\bullet}O_2-$) radicals during photoirradiation of Cu_2O crystals, and recording the generated electron paramagnetic resonance (EPR) spectra, Cu_2O rhombic dodecahedra gave stronger EPR signals than octahedra having the same total particle surface area, because more radicals were produced from photoexcited rhombic dodecahedra. The radicals were formed as a result of photogenerated electrons and holes migrating to the crystal surfaces to react with water and dissolved oxygen. Remarkably, no EPR signals were recorded from photoirradiated Cu_2O cubes. The results matched exactly with photocatalysis observations. Because no radical species are produced from photoexcited Cu_2O cubes to attack dye molecules, they show no photocatalytic activity. Strongly facet-dependent photocatalytic properties of Cu_2O crystals have been confirmed.

To trace the origin for the large photocatalytic activity variation among different crystal shapes, electron and hole scavengers were added during photodegradation of methyl orange [28]. The

scavenger test indicates both photoexcited electrons and holes in Cu_2O rhombic dodecahedra are used to form radicals for the photodegradation of methyl orange, explaining their high photocatalytic efficiency (Fig. 2c). For octahedra, mainly the excited electrons are employed to produce radical species, so octahedra are less photocatalytically active than rhombic dodecahedra. Both electrons and holes should not reach the {100} faces of Cu_2O, so cubes stay inactive. The three cases can be presented with different degrees of surface band bending. The inactive {100} face should have the largest upward bending to represent an insurmountable barrier to electron transport; electrons and holes then recombine. The most active {110} face should have the least degree of band bending to indicate facile electron transport through this surface. Although Cu_2O cubes are unsuitable for photocatalytic reactions, they may be most emissive in photoluminescence if the particles can be prepared to be ultrasmall [46]. Taken the knowledge learned from the DFT calculations of Cu_2O, the ultrathin surface layer with dissimilar band structures for the (100), (111), and (110) planes gives rise to variable degrees of surface band bending. Thus, this same surface layer affects both electronic and photocatalytic properties of Cu_2O crystals. One may recognize that the order of surface band bending for electrical conductivity and photocatalytic activity of different surfaces of Cu_2O is different (see Fig. 1b and c). How can both band diagrams be correct, since they are drawn on the basis of experimental facts? The answer may lie in the direction of current flow, which is different for the two cases. For photocatalysis, the photogenerated electrons migrate from the crystal interior to its surfaces with the particle dispersed in a solution, but current first flows from a metal wire into a crystal in electrical measurements. Even though electrons are transported across the same crystal face, different energy barriers are experienced. An analogy of this is the car window film. Although it is the same film, the person inside the car can see outside clearly, but the car interior is often invisible to a pedestrian.

Ag_2O has the same body-centered cubic crystal structure as that of Cu_2O. Ag_2O cubes, cuboctahedra, truncated octahedra, octahedra, and rhombic dodecahedra have been synthesized at room temperature using simple molar ratios of NH_4NO_3, NaOH, and $AgNO_3$ solutions [47]. Previously, Ag_2O cubes, octahedra, and rhombic dodecahedra have been used for comparative photocatalytic activity examination, showing cubes are more reactive than rhombic dodecahedra and the least active octahedra [48]. Ag_2O crystals exposing multiple faces such as hexapods were also studied for their photocatalytic properties [49]. When our synthesized Ag_2O cubes, octahedra, and rhombic dodecahedra were employed for photodegradation of methyl orange, cubes were clearly most photocatalytically active, followed by octahedra and the least active rhombic dodecahedra (see Fig. 2d). EPR spectra match well with the photocatalytic results, confirming the least but not zero activity for the Ag_2O rhombic dodecahedral particles [47]. Because both Ag_2O and Cu_2O have the same crystal structure, it is surprising that they show opposite photocatalytic activity trends. This excellent example demonstrates that explanations of facet-dependent photocatalytic activity properties in terms of surface energies and molecule-surface interactions, such as Cu atom density and molecule-surface charge consideration, are likely incorrect, since both materials should have the same surface properties including atomic arrangement [50–52]. One cannot explain both trends correctly if the surface properties follow the same order. However, DOS plots for tunable numbers of any particular Ag_2O and Cu_2O surface planes look quite different, and the number of lattice planes needed to show a gap around the Fermi level, signifying appearance of semiconductor DOS, is different for these materials [16,17]. In this regard, use of this ultrathin surface layer with dissimilar DOS profiles for Ag_2O and Cu_2O may be a better explanation for their displayed opposite photocatalytic behaviors, since barrier heights to charge migration across a particular surface of Ag_2O and Cu_2O can be different, resulting in a large difference in the amount of radical species being generated upon photoexcitation of crystals.

This thin surface layer with tunable band structures and varying degrees of band bending is also useful to explain other properties of semiconductor materials, such as the facet-dependent optical properties of Cu_2O nanocrystals, in which the Cu_2O cubes always give more red-shifted absorption and emission band positions than octahedra of similar sizes [46,53,54]. This happens because light absorption has a facet component in addition to the bulk particle absorption. The thin surface layer behaves like a film covering nanocrystals with slightly different refractive indices or dielectric constants for the {100}, {111}, and {110} faces to affect light absorption. Hence, Cu_2O polyhedra having similar sizes exhibit distinctively different colors.

Silver phosphate is another semiconductor material that can be synthesized with cubic, rhombic dodecahedral, and {111}-bound tetrahedral morphologies [29,55–57]. All these particle shapes have been reported to show efficient photodegradation of different dye molecules and photooxidation to generate oxygen [55–57]. Surprisingly, when these crystals were synthesized with room light turned off, Ag_3PO_4 tetrahedra exhibited inactivity toward photodecomposition of methyl orange, while octahedra and rhombic dodecahedra displayed moderate photocatalytic activities (Fig. 2e) [29]. EPR measurements verified the photocatalytic results, confirming practically lack of radical production upon photoexcitation of the Ag_3PO_4 tetrahedra, and low radical formation from photoirradiated rhombic dodecahedra (Fig. 2f). The significance of this example is that facet-induced photocatalytic inactivity of semiconductors may happen more often than we think, so photocatalytic deactivation of Cu_2O cubes is not a special case.

Typical semiconductor heterostructure designs for photocatalytic activity enhancement

Common strategies employed for photocatalytic activity improvement involve the formation of plasmonic metal–semiconductor heterostructures or core–shell particles with Au as a typical metal choice [45,58], decoration of metal oxide crystals with reduced graphene oxide [42,59], fabrication of semiconductor heterojunctions with favorably aligned band energies [60–69], and use of Z-scheme with usually plamonic metal nanoparticles, acting as an electron transfer mediator, placed between two semiconductor materials [70–73]. Interestingly, semiconductor heterojunction formed between CdS and Bi_2S_3 with an unfavorable band alignment can still yield photocatalytic activity enhancement because of very different interfacial electron and hole transfer rates [74]. The central idea in these designs is to promote separation of photogenerated electrons and holes through electron transfer to metal cocatalysts or graphene/graphene oxide sheets. In the case of semiconductor heterojunctions, the favorable valence and conduction band alignment of the two components should facilitate electron and hole migration across the interfaces for greater charge separation. For example, ZnS particles have been hydrothermally deposited on anatase Ti_2O nanosheets exposing {101} and {001} facets to achieve photocatalytic activity enhancement [62]. On the basis of the increased photocatalytic activities of various composites synthesized using different Zn/Ti molar ratios, as compared to those of pristine TiO_2 plates and n-type ZnS particles, it was concluded that the formation of n–p–n dual heterojunctions with p-type {001} facets of TiO_2 in contact with ZnS leads to the enhancement (see Fig. 3a,b). Such p–n heterojunction consideration does not necessarily lead to photocatalytic enhancement. Cu_2O is a p-type semiconductor. As we will see later, formation of Cu_2O–ZnS heterostructures still results in photocatalytic activity suppression [75].

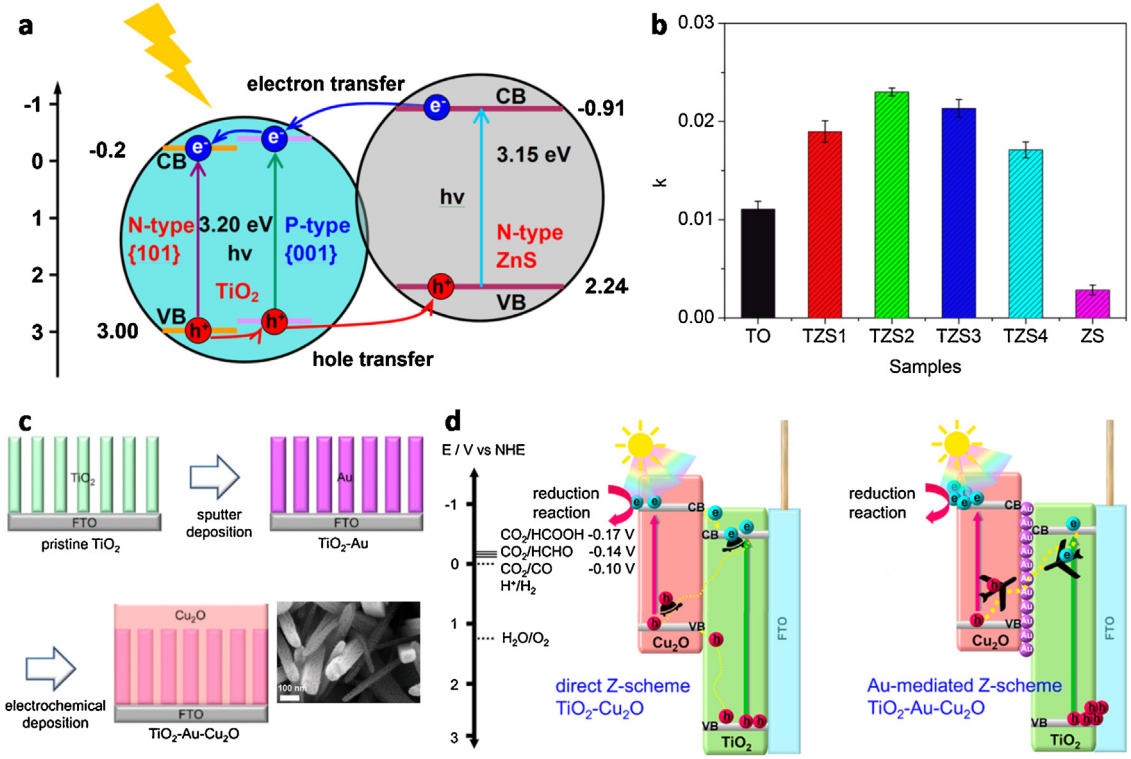

Fig. 3. (a) Schematic diagram of charge carrier transfer in TiO_2/ZnS structures. (b) Comparison of photocatalytic reaction rates of TiO_2, ZnS, and various heterostructures for methylene blue decomposition under UV–vis irradiation. Printed with permission from Ref. [62] Copyright (2017) American Chemical Society. (c) Preparation of TiO_2-Au-Cu_2O heterostructures and SEM image showing the Au-sputtered TiO_2 nanorods. (d) Proposed charge transfer mechanisms with and without Au-mediated Z-scheme. Printed with permission from Ref. [70] Copyright (2018) American Chemical Society.

For semiconductor heterostructures with Z-scheme design, Fig. 3c depicts the fabrication of TiO_2-Au-Cu_2O structure on fluorine-doped tin oxide (FTO) glass substrate [70]. Rutile TiO_2 nanorods were sputtered with a nearly continuous Au particle film, followed by electrochemical deposition of a thick Cu_2O layer covering the TiO_2 nanorods. Although the Z-scheme photocathode design with the Au film acting as an electron transfer mediator gave better photocurrent density toward photoelectrochemical CO_2 reduction and H_2 production, the enhancement was not dramatic. Here photoexcited electrons from TiO_2 and migrated holes from Cu_2O recombine at the Au interface, providing electrons in the conduction band of Cu_2O with a greater potential to carry out reduction reaction. In other Z-scheme heterostructures, the two semiconductor materials are still partially in contact with each other, showing excellent heterojunction fabrication is still challenging [76]. In such case, there is the possibility that some interfacial electron transfer can proceed without passing through the metal particles.

Interfacial plane-induced significant band bending leading to photocatalytic activity suppression in heterostructures of Cu_2O crystals deposited with ZnO, CdS, ZnS, and Ag_3PO_4

In the vast majority of literature on the photocatalytic activities of semiconductor heterostructures having favorable band alignments to facilitate photogenerated electron and hole separation, photocatalytic enhancements have mostly been reported. Although there are cases of the optimal amounts of the second semiconductor material deposited to form heterostructures with best photocatalytic performance, while addition of lesser or greater amounts of the second component led to decreased activities, the explanations offered for the variable photocatalytic responses have not been consistent and are not generally applicable [77–81]. One explanation is that the semiconductor light absorption is less if more than optimal amount of a component is added [77,82,83]. For the ZnO/TiO_2 composites, reversal of n- and p-type semiconductor properties, depending on the relative amounts of the two components, to explain the observed photocatalytic activities is unusual and hard to conceive [78]. The general impression is that photocatalytic activity improvement should occur for semiconductor heterojunctions with favorable band energy alignments as presented in the literature. Is this true? How can light absorption/penetration be partially blocked if a larger amount of the second light-absorbing semiconductor is deposited? Au/Ag–Cu_2O core–shell nanocrystals with shells of a few tens of nanometers exhibit excellent photothermal properties upon laser light irradiation, showing the plasmonic cores still absorb light efficiently [84,85]. The reality is that investigation of interfacial planes for the two contacting semiconductor materials is generally lacking in these studies, and the heterogeneous nature of the composites exposing multiple facets complicates such analysis. However, if the contacting planes at the heterojunctions are known, we may be surprised to know that photocatalytic activity suppression happen for some interfacial plane combinations.

Recognizing that Cu_2O cubes remain photocatalytically inactive even after sparse Au nanoparticle deposition, formation of semiconductor heterostructures can be examined next to see if Cu_2O cubes still show inactivity. Cu_2O cubes, octahedra, or rhombic dodecahedra were added to an ethanol solution, followed by the introduction of zinc acetate and NaOH and heating to 60 °C for 30 min to prepare ZnO–Cu_2O heterostructures [86]. The mild treatment is necessary to preserve the sharp Cu_2O faces and inhibit the formation of CuO for facet-dependent photocatalysis study. Fig. 4a shows Cu_2O cubes were still inactive after ZnO deposition toward photodegradation of methyl orange, while ZnO-decorated rhombic dodecahedra gave the expected enhancement on the basis of their

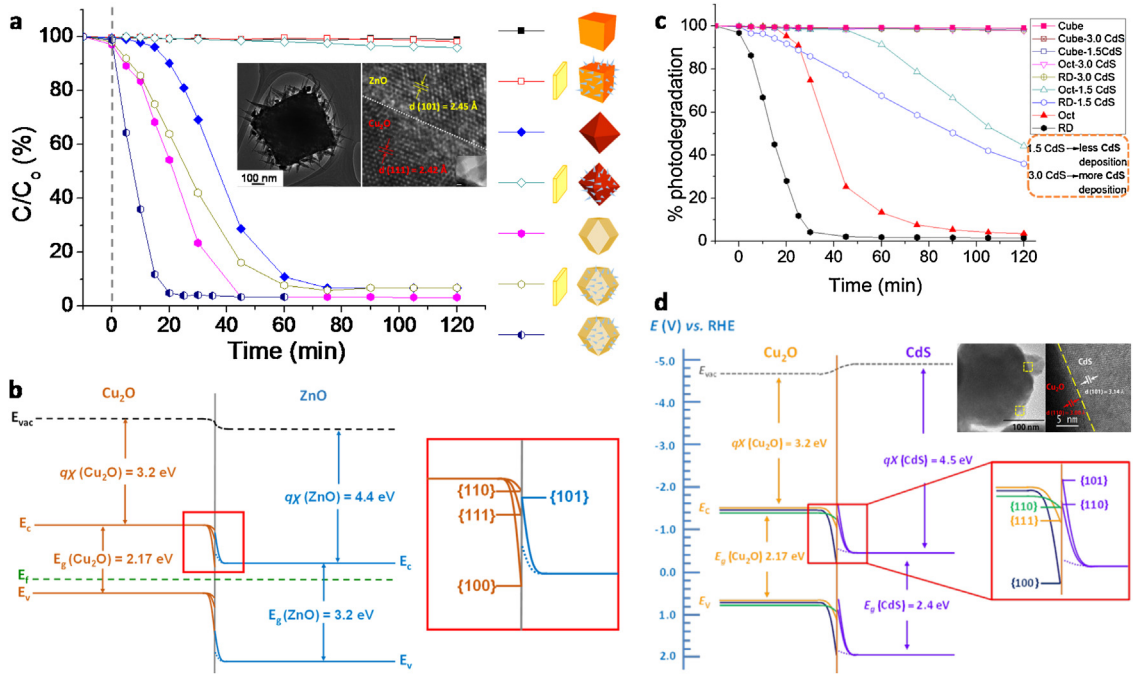

Fig. 4. (a) Extents of methyl orange photodegradation as a function of photo-irradiation time for various Cu_2O crystals and Cu_2O–ZnO heterostructures. The yellow plate represents a filter blocking UV light from reaching the reaction solution. Inset shows TEM and interfacial TEM images of the heterostructure. (b) Adjusted band diagram at the interface between Cu_2O and ZnO with consideration of relative band edge energies of different Cu_2O crystal surfaces. (a and b) Printed with permission from Ref. [86] Copyright (2017) Wiley-VCH. (c) Extents of photodegradation of MO using various Cu_2O and Cu_2O–CdS photocatalysts. (d) Adjusted band diagram of the interface between Cu_2O and CdS with consideration of relative band edge energies of different Cu_2O crystal surfaces. Inset shows interfacial TEM images of a Cu_2O–CdS rhombic dodecahedron. (c and d) Printed with permission from Ref. [75] Copyright (2018) American Chemical Society.

favorable band alignment (Fig. 4b). Remarkably, the good photocatalytic activity of octahedral Cu_2O particles became deactivated after growing ZnO on their {111} faces. XPS spectra showed no difference in the three samples. Careful interfacial TEM analysis revealed preferential growth of the (101) planes of ZnO on the (111) planes of Cu_2O (Fig. 4a). Such interfacial plane combination may induce an unexpected band bending at the heterojunction as seen in Fig. 4b. Keeping the varying degrees of surface band bending of Cu_2O in the ultrathin surface layer as before to account for their facet-dependent photocatalytic properties, the (101) planes of ZnO may bend up steeply above the energy level of the (111) planes of Cu_2O upon heterojunction formation. Specific interfacial lattice mismatch-induced strain may lead to band bending that deviates greatly from the normal extent of bending (the dash line). Under such scenario, electron transfer from Cu_2O to ZnO upon visible light illumination becomes unfavorable. DFT calculations qualitatively support this argument of elevated interfacial band energy for the {101} face of ZnO relative to that of the {111} facet of Cu_2O. Such dramatic photocatalytic deactivation is rare in the literature, suggesting the strong influence of specific interfacial plane combinations to charge transfer across semiconductor heterojunctions. Currently, it is still not possible to probe the interfacial region exclusively to derive such displaced or unmatched interfacial band bending as drawn. One also needs to contemplate what it means to interfacial band bending if significant signal variation exists between the interface region and the bulk semiconductors to explain the experimental observations. However, such picture assists our understanding of how sudden photocatalytic deactivation is possible, even though the bulk band energy alignment between Cu_2O and ZnO should promote charge separation and enhance photocatalytic performance. This example also illustrates the scope of facet-dependent properties should be expanded to include semiconductor interfaces.

To check whether photocatalytic activity suppression is broadly observable, Cu_2O–CdS heterostructures have been prepared by lightly depositing CdS nanoparticles on Cu_2O cubes, octahedra, and rhombic dodecahedra [75]. The Cu_2O crystals were dispersed in ethanol, followed by the addition of $CdCl_2$ and thioacetamide. Heating the mixture at 75 °C for 2 h yielded CdS-decorated Cu_2O crystals. Fig. 4c shows significant photocatalytic activity suppression when a smaller amount of CdS (1.5 mL of $CuCl_2$ and thioacetamide solutions each of specific concentrations) was deposited on the highly active Cu_2O rhombic dodecahedra and octahedra. Remarkably, doubling the $CuCl_2$ and thioacetamide volumes to grow more CdS on Cu_2O crystals resulted in complete photocatalytic deactivation. The Cu_2O cubes remained inactive even after CdS deposition. On the basis of band energy alignment analysis, such deactivation should not occur (Fig. 4d). In fact, one would predict all particle shapes should show enhanced photocatalytic activity. The bulk Cu_2O valence and conduction band positions were determined through Mott–Schottky and Tauc plots, showing relatively minor variations in the band positions of Cu_2O crystals exposing different surfaces. TEM analysis suggests preferential or partial growth of the (110) planes of CdS on the {111} faces of a Cu_2O octahedron, and (101) planes of CdS on the {110} faces of a Cu_2O rhombic dodecahedron (Fig. 4d). To account for the unexpected experimental observations, the interfacial CdS (110) planes is drawn to bend up steeply above the energy level of Cu_2O (111) surface planes. Similarly, the interfacial CdS (110) planes may bend up above the energy level of Cu_2O (110) surface planes. With this interfacial band bending situation, charge transfer from Cu_2O octahedra and rhombic dodecahedra to CdS becomes unfavorable. The very large downward bending for the {100} faces of Cu_2O means charge migration across this surface is inhibited regardless of which CdS lattice planes are grown on the Cu_2O cubes. This example shows that all Cu_2O particle shapes can become photocatalytically inactive with a sufficient amount of CdS deposition. There is no optimal amount of CdS giving an enhanced photocatalytic activity.

The next example is the fabrication of Cu_2O–ZnS heterostructures. To an ethanol solution of suspended Cu_2O cubes, octahedra,

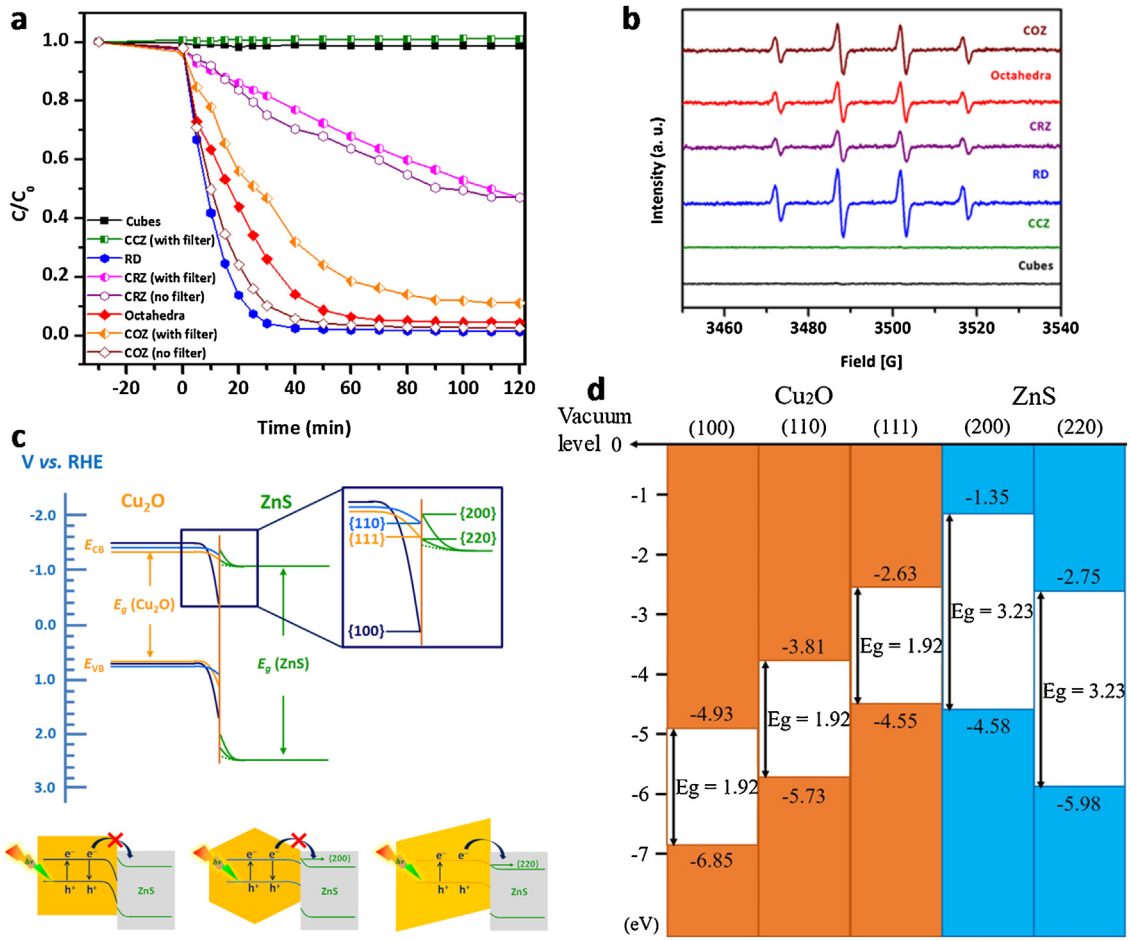

Fig. 5. (a) Extents of photodegradation of methyl orange with irradiation time for various Cu_2O crystals and Cu_2O–ZnS heterostructures. CCZ, CRZ, and COZ refer to Cu_2O cubes, rhombic dodecahedra, and octahedra with ZnS deposition, respectively. (b) EPR spectra of DMPO–OH generated from photo-irradiated Cu_2O octahedra, rhombic dodecahedra, cubes, and the Cu_2O–ZnS heterostructures. (c) Adjusted band diagram at the interface between Cu_2O and ZnS with consideration of relative band edge energies of different Cu_2O crystals. (d) DFT calculation-determined band energies of various Cu_2O and ZnS surfaces. Printed with permission from Ref. [87] Copyright (2019) American Chemical Society.

or rhombic dodecahedra was added $ZnCl_2$ and thioacetamide, and heated at 60 °C for 1 h to make the composites [87]. Fig. 5a shows the expected photocatalytic activity enhancement for ZnS-deposited Cu_2O octahedra, but significant decrease in photocatalytic activity was recorded for Cu_2O rhombic dodecahedra with sparse ZnS decoration. The Cu_2O cubes maintained inactive after surface ZnS growth. Again from band energy analysis without regard for the Cu_2O facet effects, enhanced photocatalytic activity should be observed for all the samples. EPR data confirmed the photocatalysis results, showing decreased radical formation for rhombic dodecahedra with ZnS deposition, but higher radical production in the case of ZnS-decorated Cu_2O octahedra (Fig. 5b). No radical formation explains the lack of photocatalytic activity for Cu_2O cubes with and without surface ZnS. Time-resolved photoluminescence data also indicate greater charge separation for the octahedral sample. TEM images of the interfacial regions reveal the (220) planes of ZnS run parallel to the (111) planes of Cu_2O, and the (200) planes of ZnS are aligned with the (110) planes of Cu_2O. From these results, a similar band diagram was constructed to explain photocatalytic behaviors of the various Cu_2O–ZnS heterostructures (Fig. 5c). The facet-dependent surface band bending on the Cu_2O side is kept the same as before to reflect their original photocatalytic properties. If the interfacial band bending of the (200) planes of ZnS is steep enough to reach an energy level higher than that of the {110} surface of Cu_2O, electron transport from Cu_2O to ZnS upon visible light illumination presents a barrier. With only small upward band bending on the ZnS side, electron transport across the {111} faces of Cu_2O to ZnS is facilitated. The large downward band bending for the {100} face of Cu_2O prevents excited electrons from exiting to ZnS. Interestingly, in this example photocatalytic suppression happens to Cu_2O rhombic dodecahedra, showing one cannot safely predict the outcome of interfacial charge transfer for a new heterostructure composition. DFT calculations performed to give valence and conduction band positions of Cu_2O terminated with (100), (110), and (111) planes, and those of ZnS bound by the (200) and (220) planes, support the experimental observations, showing electron transfer from the (110) planes of Cu_2O into ZnS through its (200) planes is energetically unfavorable (Fig. 5d). However, electron transfer from the (111) planes of Cu_2O to the (220) planes of ZnS should be favorable.

The last heterojunction example involves decorating Cu_2O cubes, octahedra, and rhombic dodecahedra with Ag_3PO_4 particles. After adding $AgNO_3$ to an ethanol solution of Cu_2O crystals with stirring, Na_2HPO_4 was added dropwise and stirred to obtain the heterostructures [88]. Fig. 6a summarizes the results of photodegradation of methyl orange using pristine and Ag_3PO_4-decorated Cu_2O crystals as the photocatalysts. Cu_2O cubes remained inactive despite a favorable band alignment between Cu_2O and Ag_3PO_4 (Fig. 6b). Instead of enhancement, Ag_3PO_4-decorated Cu_2O octahedra presented drastic photocatalytic activity suppression, and Cu_2O rhombic dodecahedra showed essentially photocatalytic deactivation after Ag_3PO_4 deposition. EPR spectra

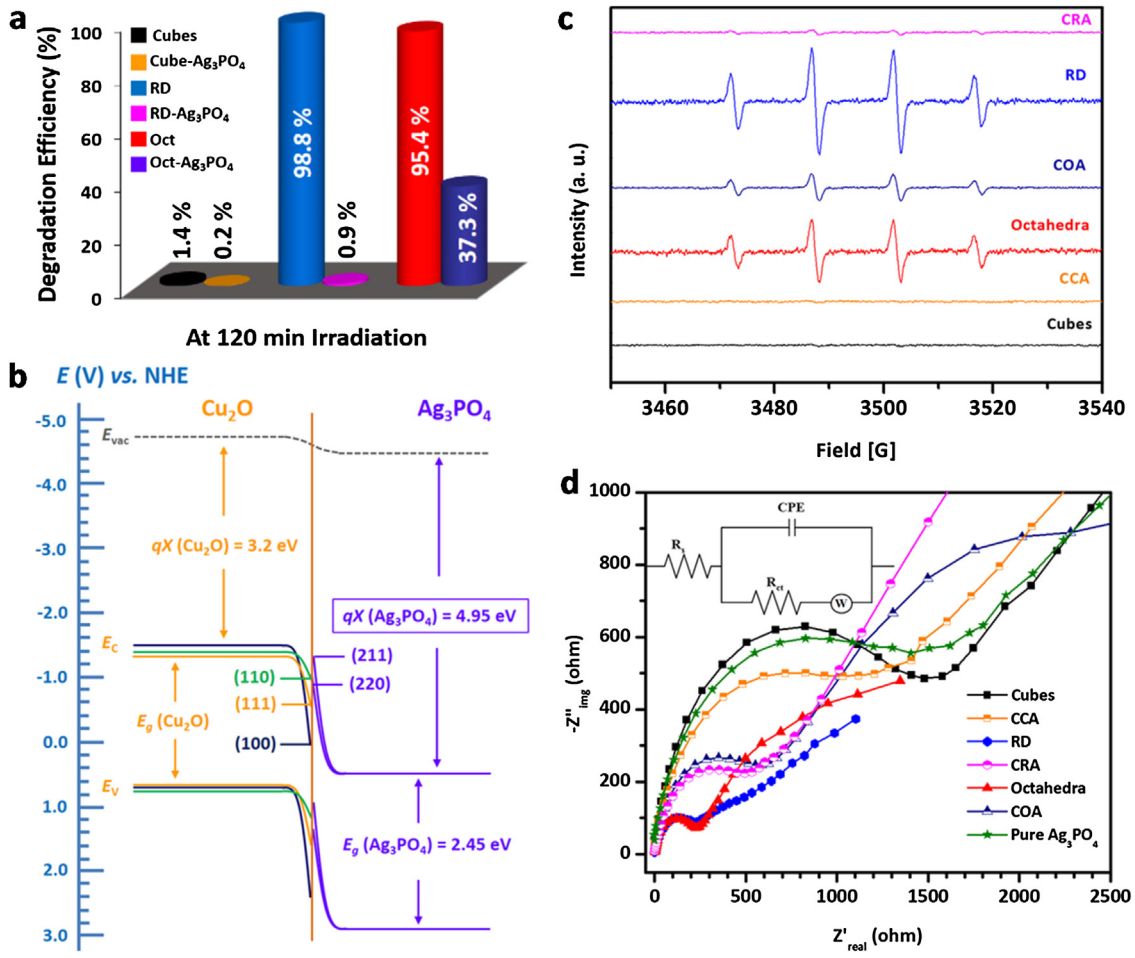

Fig. 6. (a) Photocatalytic efficiencies of Cu_2O cubes, octahedra, rhombic dodecahedra, and Cu_2O–Ag_3PO_4 heterostructures. (b) Adjusted band diagram at the interface between Cu_2O and Ag_3PO_4. (c) EPR spectra of DMPO−OH generated from photo-irradiated Cu_2O rhombic dodecahedra, octahedra, cubes, and the Cu_2O–Ag_3PO_4 heterostructures. (d) Nyquist impedance plots for various Cu_2O crystals and Cu_2O–Ag_3PO_4 heterostructures. The equivalent circuit is shown. Printed with permission from Ref. [88] Copyright (2019) American Chemical Society.

confirmed the photocatalysis results, showing decreased EPR signals for Ag_3PO_4-decorated octahedra (sample COA), nearly loss of EPR signals for Cu_2O rhombic dodecahedra after growing Ag_3PO_4 particles (CRA), and absence of EPR signals after Ag_3PO_4 deposition on Cu_2O cubes (CCA) (Fig. 6c). Nyquist impedance plots provide additional support for the significant loss of charges exiting the crystals after forming the heterostructures (Fig. 6d). The diameters of the Nyquist semicircles are much smaller for pure Cu_2O rhombic dodecahedra and octahedra, moderate for rhombic dodecahedral and octahedral Cu_2O–Ag_3PO_4 heterostructures, and far larger for Cu_2O cubes and Cu_2O–Ag_3PO_4 cubes. A sample with a larger semicircle means greater resistance for charge transfer across the particles. Again TEM characterization was carried out to determine the Ag_3PO_4 lattice planes running parallel to the various Cu_2O crystal surfaces.

From Fig. 6b, if considering the closeness in energy between the valence band of Cu_2O and the conduction band of Ag_3PO_4 to enable direct electron transfer from Ag_3PO_4 to combine with holes from Cu_2O resembling that of Z-scheme design, excited electrons from Cu_2O and holes from Ag_3PO_4 should migrate to their respective surfaces and display some photocatalytic activity or even enhanced activity. To explain the observed photocatalytic activity suppression to the point of deactivation, and in accordance with the TEM analysis, the interfacial (220) planes of Ag_3PO_4 is also drawn to rise sharply above the energy level of the (111) planes of Cu_2O, and the energy level of the interfacial Ag_3PO_4 (211) planes also climb greatly above that of the Cu_2O (110) planes. With this interfacial band alignment, charge transfer across the interface becomes unfavorable. Photocatalytic inactivity suggests the bulk semiconductor band positions is the driving force for charge migration toward the interface. But as the charges arrive at the interface, they see a barrier experienced only when they come close to it. At which point, electrons and holes can only recombine. If they migrate away from the interface in the first place, some photocatalytic activity, and even enhancement, should be recorded. This example also shows the importance of semiconductor interface to charge transport.

Conclusions and outlook

This review has shown that the electronic, photocatalytic, and optical properties of semiconductor materials are generally highly facet-dependent. All these phenomena are related, and can be explained in terms of the presence of an ultrathin surface layer with dissimilar surface band structures and hence tunable degrees of band bending. For charge transport, this means they see different barrier heights at various crystal surfaces. After all, if Cu_2O crystals can be simultaneously highly conductive and insulating, we should not be so surprised that complete photocatalytic activity deactivation can occur. For optical properties, nanocrystals exposing various facets should have slightly different surface refractive indices or dielectric constants. When plasmons and photons passing through this layer, the nanocrystal absorption and emission band positions are tuned accordingly.

When semiconductor heterojunctions are formed, large band bending on both sides of the interface can happen, making the heterostructures photocatalytically suppressed or completely deactivated. The photocatalytic outcome greatly depends on the contacting planes, so the scope of surface facet effects should extend to semiconductor heterojunctions. Although photocatalytic activity decrease upon heterojunction formation seems less interesting and often gets ignored, it is nevertheless part of the photocatalytic mechanism and intrinsic properties of semiconductor materials. More reports addressing photocatalytic activity suppression should give us more complete understanding of semiconductor materials. On the other hand, we may turn this unwanted behavior into opportunities. For example, charge recombination may give stronger emission intensities, as has been suggested in ultrasmall Cu_2O nanocubes [46,89]. Thus, semiconductor particles of a certain shape may give brighter photoluminescence than another shape of comparable size. Furthermore, if plane-specific semiconductor heterojunctions can facilitate or inhibit charge migration across the interface, it should be interesting to see what this would do to the electronic properties of such junctions, and how light irradiation on the heterojunction affects their electrical responses. These are some research possibilities that may not be conceived without recognizing the prevalence of photocatalytic suppression in Cu_2O-based semiconductor heterostructures.

Acknowledgment

We thank the Ministry of Science and Technology of Taiwan for the financial support of this work (MOST 107-2113-M-007-013-MY3 and 107-3017-F-007-002).

References

[1] M.H. Huang, G. Naresh, H.-S. Chen, ACS Appl. Mater. Interfaces 10 (2018) 4–15.
[2] S. Bai, L. Wang, Z. Li, Y. Xiong,Adv. Sci. 4 (2017), 1600216.
[3] M.H. Huang, S. Rej, S.-C. Hsu, Chem. Commun. 50 (2014) 1634–1644.
[4] C.W. Kim, S.J. Yeob, H.-M. Cheng, Y.S. Kang, Energy Environ. Sci. 8 (2015) 3646–3653.
[5] G. Liu, L.-C. Yin, J. Pan, F. Li, L. Wen, C. Zhen, H.-M. Cheng, Adv. Mater. 27 (2015) 3507–3512.
[6] S. Wang, G. Liu, L. Wang, Chem. Rev. 119 (2019) 5192–5247.
[7] S.-H. Liu, J.-S. Lu, Y.-C. Pu, H.-C. Fan, J. CO_2 Util. 33 (2019) 171–178.
[8] P.-L. Hsieh, G. Naresh, Y.-S. Huang, C.-W. Tsao, Y.-J. Hsu, L.-J. Chen, M.H. Huang, J. Phys. Chem. C 123 (2019) 13664–13671.
[9] Y.B. Vogel, V.R. Gonçales, J.J. Gooding, S. Ciampi, J. Electrochem. Soc. 165 (2018) H3085–H3092.
[10] K. Chanda, S. Rej, M.H. Huang, Chem. Eur. J. 19 (2013) 16036–16043.
[11] K. Chanda, S. Rej, M.H. Huang, Nanoscale 5 (2013) 12494–12501.
[12] H.-Y. Tsai, M. Madasu, M.H. Huang, Chem. Eur. J. 25 (2019) 1300–1303.
[13] P. Losch, W. Huang, E.D. Goodman, C.J. Wrasman, A. Holm, A.R. Riscoe, J.A. Schwalbe, M. Cargnello, Nano Today 24 (2019) 15–47.
[14] R. Wang, N. Sakai, A. Fujishima, T. Watanabe, K. Hashimoto, J. Phys. Chem. B 103 (1999) 2188–2194.
[15] M. Miyauchi, A. Shimai, Y. Tsuru, J. Phys. Chem. B 109 (2005) 13307–13311.
[16] C.-S. Tan, S.-C. Hsu, W.-H. Ke, L.-J. Chen, M.H. Huang, Nano Lett. 15 (2015) 2155–2160.
[17] C.-S. Tan, Y.-J. Chen, C.-F. Hsia, M.H. Huang, Chem. Asian J. 12 (2017) 293–297.
[18] C.-S. Tan, H.-S. Chen, C.-Y. Chiu, S.-C. Wu, L.-J. Chen, M.H. Huang, Chem. Mater. 28 (2016) 1574–1580.
[19] C.-S. Tan, M.H. Huang, Chem. Eur. J. 23 (2017) 11866–11871.
[20] C.-S. Tan, M.H. Huang, Chem. Asian J. 13 (2018) 1972–1976.
[21] C.-S. Tan, M.H. Huang, Chem. Asian J. 14 (2019) 2316–2321.
[22] S.Y. Leblebici, L. Leppert, Y. Li, S.E. Reyes-Lillo, S. Wickenburg, E. Wong, J. Lee, M. Melli, D. Ziegler, D.K. Angell, D.F. Ogletree, P.D. Ashby, F.M. Toma, J.B. Neaton, I.D. Sharp, A. Weber-Bargioni, Nat. Energy 1 (2016) 16093.
[23] P. Ilanchezhiyan, G.M. Kumar, F. Xiao, A. Madhankumar, C. Siva, S.U. Yuldashev, H.D. Cho, T.W. Kang, Sol. Energy Mater. Sol. Cells 183 (2018) 73–81.
[24] C. Ran, W. Gao, N. Li, Y. Xia, Q. Li, Z. Wu, H. Zhou, Y. Chen, M. Wang, W. Huang, ACS Energy Lett. 4 (2019) 358–367.
[25] T. Egawa, B.A.B. Ahmad Shuhaimi,J. Phys. D Appl. Phys. 43 (2010), 354008.
[26] S. Hu, S. Liu, Z. Zhang, H. Yan, Z. Gan, H. Fang, J. Cryst. Growth 415 (2015) 72–77.
[27] C.-H. Kuo, Y.-C. Yang, S. Gwo, M.H. Huang, J. Am. Chem. Soc. 133 (2011) 1052–1057.
[28] C.-Y. Chu, M.H. Huang, J. Mater. Chem. A 5 (2017) 15116–15123.
[29] M.-S. Hsieh, H.-J. Su, P.-L. Hsieh, Y.-W. Chiang, M.H. Huang, ACS Appl. Mater. Interfaces 9 (2017) 39086–39093.
[30] C.-S. Tan, P.-L. Hsieh, L.-J. Chen, M.H. Huang, Angew. Chem. Int. Ed. 56 (2017) 15339–15343.
[31] P.-L. Hsieh, A.-T. Lee, L.-J. Chen, M.H. Huang, Angew. Chem. Int. Ed. 57 (2018) 16162–16165.
[32] Y.B. Vogel, J. Zhang, N. Darwish, S. Ciampi, ACS Nano 12 (2018) 8071–8080.
[33] Y.B. Vogel, V.R. Gonçales, L. Al-Obaidi, J.J. Gooding, N. Darwish, S. Ciampi,Adv. Funct. Mater. 28 (2018), 1804791.
[34] Y. Hou, X.Y. Li, Q.D. Zhao, X. Quan, G.H. Chen,Appl. Phys. Lett. 95 (2009), 093108.
[35] W. Lei, T. Zhang, L. Gu, P. Liu, J.A. Rodriguez, G. Liu, M. Liu, ACS Catal. 5 (2015) 4385–4393.
[36] Y.L. Wang, Y.H. Li, X.L. Wang, Y. Hou, A.P. Chen, H.G. Yang, Appl. Catal. B 206 (2017) 216–220.
[37] M. Meng, X. Wu, X. Zhu, L. Yang, Z. Gan, X. Zhu, L. Liu, P.K. Chu, J. Phys. Chem. Lett. 5 (2014) 4298–4304.
[38] W.-C. Huang, L.-M. Lyu, Y.-C. Yang, M.H. Huang, J. Am. Chem. Soc. 134 (2012) 1261–1267.
[39] Y. Zhang, B. Deng, T. Zhang, D. Gao, A.-W. Xu, J. Phys. Chem. C 114 (2010) 5073–5079.
[40] W.-C. Wang, L.-M. Lyu, M.H. Huang, Chem. Mater. 23 (2011) 2677–2684.
[41] D. Jiang, W. Zhou, X. Zhong, Y. Zhang, X. Li, ACS Appl. Mater. Interfaces 6 (2014) 10958–10962.
[42] Y.-C. Pu, H.-Y. Chou, W.-S. Kuo, K.-H. Wei, Y.-J. Hsu, Appl. Catal. B 204 (2017) 21–32.
[43] A.E. Kandjani, Y.M. Sabri, S.R. Periasamy, N. Zohora, M.H. Amin, A. Nafady, S.K. Bhargava, Langmuir 31 (2015) 10922–10930.
[44] Y. Liang, L. Shang, T. Bian, C. Zhou, D. Zhang, H. Yu, H. Xu, Z. Shi, T. Zhang, L.-Z. Wu, C.-H. Tung, CrystEngComm 14 (2012) 4431–4436.
[45] G.-Z. Yuan, C.-F. Hsia, Z.-W. Lin, C. Chiang, Y.-W. Chiang, M.H. Huang, Chem. Eur. J. 22 (2016) 12548–12556.
[46] J.-Y. Huang, M. Madasu, M.H. Huang, J. Phys. Chem. C 122 (2018) 13027–13033.
[47] Y.-J. Chen, Y.-W. Chiang, M.H. Huang, ACS Appl. Mater. Interfaces 8 (2016) 19672–19679.
[48] G. Wang, X. Ma, B. Huang, H. Cheng, Z. Wang, J. Zhan, X. Qin, X. Zhang, Y. Dai, J. Mater. Chem. 22 (2012) 21189–21194.
[49] Y.-W. Harn, T.-H. Yang, T.-Y. Tang, M.-C. Chen, J.-M. Wu, ChemCatChem 7 (2015) 80–86.
[50] Y. Shang, L. Guo,Adv. Sci. 2 (2015), 1500140.
[51] Y.-K. Peng, S.C.E. Tsang, Nano Today 18 (2018) 15–34.
[52] Y. Su, H. Li, H. Ma, J. Robertson, A. Nathan, ACS Appl. Mater. Interfaces 9 (2017) 8100–8106.
[53] M.H. Huang,Small 15 (2019), 1804726.
[54] W.-H. Ke, C.-F. Hsia, Y.-J. Chen, M.H. Huang, Small 12 (2016) 3530–3534.
[55] Y. Bi, S. Ouyang, N. Umezawa, J. Cao, J. Ye, J. Am. Chem. Soc. 133 (2011) 6490–6492.
[56] D.J. Martin, N. Umezawa, X. Chen, J. Ye, J. Tang, Energy Environ. Sci. 6 (2013) 3380–3386.
[57] B. Zheng, X. Wang, C. Liu, K. Tan, Z. Xie, L. Zheng, J. Mater. Chem. A 1 (2013) 12635–12640.
[58] M.-Y. Kuo, C.-F. Hsiao, Y.-H. Chiu, T.-H. Lai, M.-J. Fang, J.-Y. Wu, J.-W. Chen, C.-L. Wu, K.-H. Wei, H.-C. Lin, Y.-J. Hsu, Appl. Catal. B 242 (2019) 499–506.
[59] Y. Tang, X. Liu, C. Ma, M. Zhou, P. Huo, L. Yu, J. Pan, W. Shi, Y. Yan, New J. Chem. 39 (2015) 5150–5160.
[60] H. Wang, L. Zhang, Z. Chen, J. Hu, S. Li, Z. Wang, J. Liu, X. Wang, Chem. Soc. Rev. 43 (2014) 5234–5244.
[61] J. Theerthagiri, S. Chandrasekaran, S. Salla, V. Elakkiya, R.A. Senthil, P. Nithyadharseni, T. Maiyalagan, K. Michael, A. Ayeshamariam, M.V. Arasu, N.A. Al-Dhabi, H.-S. Kim, J. Solid State Chem. 267 (2018) 35–52.
[62] J. Zhang, X. Ma, L. Zhang, Z. Lu, E. Zhang, H. Wang, Z. Kong, J. Xi, Z. Ji, J. Phys. Chem. C 121 (2017) 6133–6140.
[63] C. Yu, G. Li, S. Kumar, K. Yang, R. Jin, Adv. Mater. 26 (2014) 892–898.
[64] X.-J. Wen, C.-G. Niu, L. Zhang, C. Liang, G.-M. Zeng, Appl. Catal. B 221 (2018) 701–714.
[65] C. Wang, B. Ma, X. Cao, S. He, J. Han, M. Wei, D.G. Evans, X. Duan, J. Mater. Chem. A 6 (2018) 7871–7876.
[66] K.H. Reddy, K. Parida, P.K. Satapathy, J. Mater. Chem. A 5 (2017) 20359–20373.
[67] W. Zhao, Y. Liu, Z. Wei, S. Yang, H. He, C. Sun, Appl. Catal. B 185 (2016) 242–252.
[68] D. Ma, J.-W. Shi, Y. Zou, Z. Fan, J. Shi, L. Cheng, D. Sun, Z. Wang, C. Niu, Nanoscale 10 (2018) 7860–7870.
[69] X. Li, M. Su, G. Zhu, K. Zhang, X. Zhang, J. Fan, Dalton Trans. 47 (2018) 10046–10056.
[70] J.-M. Li, C.-W. Tsao, M.-J. Fang, C.-C. Chen, C.-W. Liu, Y.-J. Hsu, ACS Appl. Nano Mater. 1 (2018) 6843–6853.
[71] F. Chen, Q. Yang, X. Li, G. Zeng, D. Wang, C. Niu, J. Zhao, H. An, T. Xie, Y. Deng, Appl. Catal. B 200 (2017) 330–342.
[72] T. Di, Q. Xu, W. Ho, H. Tang, Q. Xiang, J. Yu, ChemCatChem 11 (2019) 1394–1411.
[73] D. Zheng, C. Pang, X. Wang, Chem. Commun. 51 (2015) 17467–17470.
[74] Z. Fang, Y. Liu, Y. Fan, Y. Ni, X. Wei, K. Tang, J. Shen, Y. Chen, J. Phys. Chem. C 115 (2011) 13968–13976.
[75] J.-Y. Huang, P.-L. Hsieh, G. Naresh, H.-Y. Tsai, M.H. Huang, J. Phys. Chem. C 122 (2018) 12944–12950.

[76] J.-M. Li, H.-Y. Cheng, Y.-H. Chiu, Y.-J. Hsu, Nanoscale 8 (2016) 15720–15729.
[77] X. Guan, L. Guo, ACS Catal. 4 (2014) 3020–3026.
[78] W. Sun, S. Meng, S. Zhang, X. Zheng, X. Ye, X. Fu, S. Chen, J. Phys. Chem. C 122 (2018) 15409–15420.
[79] S. Chen, W. Zhao, W. Liu, H. Zhang, X. Yu, Y. Chen, J. Hazard. Mater. 172 (2009) 1415–1423.
[80] J. Wang, J. Jin, X. Wang, S. Yang, Y. Zhao, Y. Wu, S. Dong, J. Sun, J. Sun, J. Colloid Interfaces Sci. 505 (2017) 805–815.
[81] Y. Bessekhouad, D. Robert, J.-V. Weber, Catal. Today 101 (2005) 315–321.
[82] Y. Cui, L. Pan, Y. Chen, N. Afzal, S. Ullah, D. Liu, L. Wang, X. Zhang, J.-J. Zou, RSC Adv. 9 (2019) 5492–5500.
[83] Y. Fan, M. Deng, G. Chen, Q. Zhang, Y. Luo, D. Li, Q. Meng, J. Alloys. Compd. 509 (2011) 1477–1481.
[84] H.-J. Wang, K.-H. Yang, S.-C. Hsu, M.H. Huang, Nanoscale 8 (2016) 965–972.
[85] K.-H. Yang, S.-C. Hsu, M.H. Huang, Chem. Mater. 28 (2016) 5140–5146.
[86] S.-C. Wu, C.-S. Tan, M.H. Huang,Adv. Funct. Mater. 27 (2017), 1604635.
[87] G. Naresh, P.-L. Hsieh, V. Meena, S.-K. Lee, Y.-H. Chiu, M. Madasu, A.-T. Lee, H.-Y. Tsai, T.-H. Lai, Y.-J. Hsu, Y.-C. Lo, M.H. Huang, ACS Appl. Mater. Interfaces 11 (2019) 3582–3589.
[88] G. Naresh, A.-T. Lee, V. Meena, M. Satyanarayana, M.H. Huang, J. Phys. Chem. C 123 (2019) 2314–2320.
[89] S. Thoka, A.-T. Lee, M.H. Huang, ACS Sustain. Chem. Eng. 7 (2019) 10467–10476.

Michael H. Huang is a professor in the Department of Chemistry, National Tsing Hua University. Since August 2018, he has become a distinguished professor of NTHU. His current research interests focus on the synthesis of semiconductor nanocrystals with tunable shapes and the examination of various facet-dependent properties of semiconductor materials.

Mahesh Madasu has received his B.Sc. degree from Kakatiya University, India, in 2009 and Master's degree from the Department of Chemistry, Indian Institute of Technology Bombay, India, in 2012. From 2012 to 2014, he worked as a Junior Research Fellow at IIT Bombay. In 2018, he received a Ph.D. degree from the Department of Chemistry, National Tsing Hua University under the guidance of Prof. Michael. H. Huang. Currently, he is working as a postdoctoral fellow in Prof. Michael. H. Huang's lab. His research work is mainly focused on the formation of polyhedral metal nanocrystals formed from pseudomorphic conversion of semiconductor nanocrystals and their catalytic applications.